



## Full Text View

[Volume 29, Issue 7 \(July 1999\)](#)

### Journal of Physical Oceanography

Article: pp. 1599–1618 | [Abstract](#) | [PDF \(590K\)](#)

# Intraseasonal Variability in the Indo–Pacific Throughflow and the Regions Surrounding the Indonesian Seas

**Bo Qiu, Ming Mao, and Yuji Kashino\***

*Department of Oceanography, University of Hawaii at Manoa, Honolulu, Hawaii*

(Manuscript received March 27, 1998, in final form September 15, 1998)

DOI: 10.1175/1520-0485(1999)029<1599:IVITIP>2.0.CO;2

## ABSTRACT

Intraseasonal oscillations in sea level, sea surface temperature, and upper ocean flow field have recently been observed in various locations surrounding the Indonesian seas. While the observed oscillations at these locations have similar wave periods ranging from 30 to 85 days, their forcing mechanisms can involve different dynamic processes. In order to clarify the dynamic processes essential for the observed intraseasonal signals, the authors adopted in this study a fine-resolution 1½-layer reduced-gravity model and carried out a series of model experiments by varying coastline geometry and surface wind forcing. From these carefully designed experiments, they show that the intense 50-day oscillations observed at the entrance of Celebes Sea are a result of Rossby wave resonance in which the frequency of cyclonic eddy shedding by the retroflecting Mindanao Current matches that of the gravest Rossby mode of the semi-enclosed Celebes Sea basin. These 50-day oscillations of the Celebes Sea have a large impact on the throughflow in the Makassar Strait and Banda Sea, but do not contribute significantly to the throughflow changes in the Lombok, Ombai, and Timor Straits.

The observed intraseasonal signals along the Sumatra/Java coasts in the eastern Indian Ocean are dominated by oscillations with wave periods of 50 and 85 days. The origin of these wave signals can be traced back to the central equatorial Indian Ocean where the surface zonal wind fluctuates intraseasonally with the same wave periods. The remotely induced coastal Kelvin waves along the Sumatra/Java coasts strongly influence the Lombok Strait, but exert no direct influence upon the Ombai and Timor Straits farther to the east; the gap of the Lombok Strait is found to conduit the Kelvin wave signals effectively into the Makassar Strait and the Banda Sea. The intraseasonal signals observed in the Timor Passage have a dominant wave period of 30–35 days. The model simulation further suggests the presence of a second spectral peak around 85 days. Both of these intraseasonal signals are attributable to the local, along-archipelago wind near the Timor Passage.

### Table of Contents:

- [Introduction](#)
- [The model](#)
- [Results of the base model](#)
- [Intraseasonal variability](#)
- [Intraseasonal variability](#)
- [Summary](#)
- [REFERENCES](#)
- [TABLES](#)
- [FIGURES](#)

### Options:

- [Create Reference](#)
- [Email this Article](#)
- [Add to MyArchive](#)
- [Search AMS Glossary](#)


### Search CrossRef for:

- [Articles Citing This Article](#)


### Search Google Scholar for:

- [Bo Qiu](#)
- [Ming Mao](#)
- [Yuji Kashino](#)

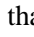
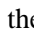
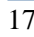
## 1. Introduction

Our understanding of the ocean circulation in the Indonesian archipelago region has improved considerably over the past decade. Recognition that the Indonesian Throughflow (ITF) is not only crucial to the heat and freshwater balance in the Indian Ocean but also plays an important role in the global circulation of thermocline water ([Godfrey and Golding 1981](#); [Piola and Gordon 1984](#); [Gordon 1986](#); [Broecker 1991](#)) has led to increased interest in this region of the World Ocean ([Fig. 1](#) ). Most of the past observational, numerical, and theoretical studies have focused on the transport value of the ITF, as well as its seasonal-to-interannual fluctuations. As presented in a recent comprehensive review by [Godfrey \(1996\)](#), estimates for the throughflow transport ranged from nil to 20 Sv ( $\text{Sv} \equiv 10^6 \text{ m}^3 \text{ s}^{-1}$ ), depending on the data and methodology used. A recent estimate based on long-term expandable bathythermograph (XBT) observations by [Meyers et al. \(1995\)](#) placed the mean throughflow transport at 7 Sv for the upper 400 m of the water column.

The annual cycle of the ITF, with a maximum transport in boreal summer and a minimum in boreal winter, is well established from observations ([Wyrki 1987](#); [Murray and Arief 1988](#); [Meyers et al. 1995](#); [Molcard et al. 1996](#)). Several studies have attributed this transport cycle to the seasonal fluctuations of the Asian–Australian monsoonal wind; namely, the ITF is strongest during the southeast monsoon from May to September and it is weaker during the northwest monsoon from November to March (e.g., [Kindle et al. 1989](#); [Inoue and Welsh 1993](#); [Masumoto and Yamagata 1993](#); [Clarke and Liu 1993](#); [Miyama et al. 1995](#); [Yamagata et al. 1996](#)). Interannually, the ITF transport is found to be closely connected to Pacific ENSO events, and the correlation is such that a smaller than normal ITF transport is found in El Niño years and a larger transport in La Niña years (e.g., [Kindle et al. 1989](#); [Clarke and Liu 1994](#); [Wajsowicz 1994](#); [Verschell et al. 1995](#); [Meyers 1996](#); [Potemra et al. 1997](#)). The peak-to-trough amplitude of the ENSO-related transport changes is estimated to be about 5 Sv ([Meyers 1996](#)).

Compared to the seasonal-to-interannual signals, throughflow variability with the intraseasonal timescale has heretofore received less attention. Given the shallow water depth and the complex coastline geometry of the archipelago, short-term current fluctuations are likely to be important for the regional mixing and water mass transformation of the ITF. This study focusing on the ITF's intraseasonal variability is motivated by several recent observational studies. From current meter moorings at the Pacific entrance of the Celebes Sea around 4.0°N, 127.5°E, [Watanabe et al. \(1997\)](#) and [Kashino et al. \(1999\)](#) recently observed strong 50- to 60-day oscillations in the Mindanao Current just before it enters the Celebes Sea and forms the “western route” of the ITF ([Field and Gordon 1992](#)). The observed intraseasonal oscillation is clearest at the 350-m depth, but also detectable deeper at 550 m, and persisted throughout the 14-month period of the mooring measurements ([Fig. 2](#) ). It is interesting to note that the observed intraseasonal fluctuations have opposite phases between these two depths, indicating a baroclinic nature of the intraseasonal signals.

Within the Indonesian seas, [Field and Gordon \(1996\)](#) analyzed the weekly SST data compiled by the Climate Analysis Center and found the dominant SST changes in the intraseasonal frequency band there are around 60 days. These 60-day signals can be detected in almost all subregions of the Indonesian seas; Field and Gordon suggested that the 60-day periodicity might be a harmonic of the monthly tidal signal or reflect the atmospheric Madden–Julian oscillation (MJO).

Intraseasonal fluctuations have been detected at the exit side of the ITF in the Indian Ocean as well. From current meter moorings deployed across the Timor Passage, [Molcard et al. \(1996\)](#) observed successions of current oscillations with wave periods ranging from 20 to 60 days. Their empirical orthogonal function (EOF) analysis on the alongchannel flow revealed that most of the 20 to 60 day variability is contained in the upper 500 m of the ocean. [Figure 3a](#)  shows the time series of the first EOF mode obtained by Molcard et al. from the mooring data at 11.3°S, 122.9°E. The EOF mode contains 37% of the signal variance and has a surface-intensified, first baroclinic mode structure (for details, see [Fig. 8](#)  of [Molcard et al. 1996](#)). The power spectra of this time series show that the dominant intraseasonal signals have energy peaks around 35 and 17 days ([Fig. 3b](#) ). Similar spectral peaks have also been detected by [Molcard et al. \(1994\)](#) in their earlier mooring observations in the Timor Passage from August 1989 to July 1990.

Along the Java coast, intraseasonal signals in the 40–60-day band were noted by [Arief and Murray \(1996\)](#) in their analysis of tide gauge sea level data. From lagged regression analysis, Arief and Murray showed that these observed oscillations exhibited characteristics of baroclinic coastal Kelvin waves originating from the equatorial Indian Ocean and that they had a direct impact on the observed ITF outflow in Lombok Strait. More recently, [Bray et al. \(1997\)](#) have detected energetic eddies and meanders in the current system south of Java with 60-day intraseasonal changes in the surface dynamic height field. The observed intraseasonal signals were comparable in magnitude to the seasonal and interannual signals and they accounted for much of the variation in water mass properties between hydrographic cruises.

It is worth noting that intraseasonal signals of 40–60 days are also present in some of the simulation models focusing on either the global ocean circulation or the regional circulation in the tropical Pacific western boundary and the Indonesian

archipelago. For example, [Ponte and Gutzler \(1992\)](#) analyzed the [Semtner and Chervin \(1992\)](#) eddy-resolving general circulation model output and found the presence of energetic 40–60 day oscillations in both the western equatorial Pacific and the eastern equatorial Indian Oceans. Similarly, intraseasonal variability in the Mindanao Current along the Philippine coast has been identified in regional modeling studies by [Inoue and Welsh \(1993\)](#), see their [Fig. 10](#) and by [Qiu and Lukas \(1996\)](#), their [Fig. 12b](#). As these modeling studies were mainly concerned with the lower-frequency (annual to interannual) changes of the ocean circulation, a thorough investigation focusing on the dynamic processes underlying the intraseasonal variability is lacking.

Understanding the intraseasonal variability in the region surrounding the Indonesian archipelago is complex for several reasons. First, this region is where the MJO has its strongest surface wind signals (for a recent review of the observational aspects of the MJOs, see [Madden and Julian 1994](#)). A question arising immediately is to what extent the observed intraseasonal signals in the ocean are a consequence of direct atmospheric forcing. Second, the Indonesian archipelago is located in pathways of equatorial and coastal waveguides; as a result, ocean circulation is subject to regional surface wind forcing as well as remote surface wind forcing. Third, the complicated coastline geometry in the region, when interacting with the seasonally varying throughflow, can both regulate and enhance current fluctuations in the intraseasonal frequency band.

The objective of this study is to use a fine-resolution, 1½-layer reduced-gravity model forced by the observed wind to clarify the nature and causes of the intraseasonal signals found in the aforementioned observational studies. Though simple in its formulation, the 1½-layer reduced-gravity model has been used successfully in the past to simulate the tropical and subtropical circulations in the Pacific and Indian Oceans (e.g., [Kindle et al. 1989](#); [Woodberry et al. 1989](#); [Hurlburt et al. 1989](#); [Inoue and Welsh 1993](#); [Verschell et al. 1995](#); among others). It is worth emphasizing that the reduced-gravity model adopted in this study contains the essential physics for reproducing the intraseasonal signals similar to the observations. Through a series of model experiments with different surface wind forcing and coastal geometries, we will address the three issues listed above that are relevant to the intraseasonal signals in the Indonesian archipelago regions.

The presentation of this paper is organized as follows. In [section 2](#), we start with a brief description of the numerical model. [Section 3](#) focuses on the simulated ITF’s variability: its seasonal and intraseasonal signals and its comparison with available observations. In [section 4](#), we will explore the physics underlying the observed and modeled intraseasonal variability with an emphasis on the Pacific entrance region of the ITF. Intraseasonal variability of the throughflow in the Indian Ocean outflow region is investigated in [section 5](#). [Section 6](#) summarizes the results from the present study.

## 2. The model

The numerical model used in this study is a 1½-layer reduced-gravity model that incorporates the mixed layer physics of [Kraus and Turner \(1967\)](#). As the model’s dynamics and thermodynamics closely follow those described by [McCreary and Kundu \(1989\)](#), only a concise description is included below. Dynamically, the model consists of an active upper layer and an underlying infinitely deep abyssal layer. Equations governing the motion in the upper layer are

$$\frac{\partial \mathbf{u}}{\partial t} + \mathbf{u} \cdot \nabla \mathbf{u} + f \mathbf{k} \times \mathbf{u} = -\overline{\nabla p} + \frac{\boldsymbol{\tau}}{\rho_o h} + A_h \nabla^2 \mathbf{u}, \quad (1)$$

$$\frac{\partial h}{\partial t} + \nabla \cdot (h \mathbf{u}) = K_h \nabla^2 h + w_e, \quad (2)$$

where  $\mathbf{u}$  is the velocity vector in the upper layer,  $h$  is the upper-layer thickness,  $\mathbf{k}$  is a unit vector in the vertical direction,  $A_h$  ( $K_h$ ) is the coefficient of the horizontal eddy viscosity (diffusivity),  $f$  is the Coriolis parameter,  $\boldsymbol{\tau}$  is the surface wind stress vector, and  $\rho_o$  is the reference water density. The entrainment velocity  $w_e$  in [Eq. \(2\)](#) is given by

$$w_e = \begin{cases} w_s, & h > h_m \\ w_s + w_K, & h = h_m, \end{cases} \quad (3)$$

where  $h_m$  is the thickness of the surface mixed layer and  $w_s$  denotes the shear entrainment and is operative if  $h$  becomes less than a prescribed “entrainment depth”  $H_e$ :

where  $t_e$  is a specified relaxation time. In [Eq. \(3\)](#),  $w_K$  denotes the Kraus and Turner entrainment due to wind stirring and surface cooling (for details, see [McCreary and Kundu 1989](#)).

Within the dynamic upper layer, a surface mixed layer of thickness  $h_m$  and temperature  $T_m$  exists above a fossil sublayer of thickness  $h_f$  ( $\equiv h - h_m$ ) and temperature  $T_f$ . By requiring the horizontal pressure gradient to vanish in the abyssal layer, we can express the  $\overline{\nabla p}$  term in [Eq. \(1\)](#) associated with the horizontal temperature changes in the upper layer as follows:

$$\overline{\nabla p} = \alpha g \nabla (T - T_d) h - \frac{1}{2} \alpha g h \nabla T,$$

where  $\alpha$  is the thermal expansion coefficient,  $g$  is the gravity constant,  $T = (h_m T_m + h_f T_f)/h$  is the vertically averaged temperature in the upper layer, and  $T_d$  is the temperature of the abyssal ocean.

Equations governing the temporal evolution of the mixed layer depth and the mixed layer and fossil layer temperatures are

$$\frac{\partial h_m}{\partial t} + \nabla \cdot (h_m \mathbf{u}) = K_h \nabla^2 h_m + w_K, \quad (4)$$

$$\begin{aligned} \frac{\partial T_m}{\partial t} + \mathbf{u} \cdot \nabla T_m &= K_h \nabla^2 T_m + \frac{Q}{\rho_o c_p h_m} \\ &+ \text{entrainment}, \end{aligned} \quad (5)$$

$$\frac{\partial T_f}{\partial t} + \mathbf{u} \cdot \nabla T_f = K_h \nabla^2 T_f + \text{entrainment}, \quad (6)$$

where  $Q$  is surface heat flux and  $c_p$  is the specific heat of seawater. The detailed expressions for the entrainment terms in [Eqs. \(5\)](#) and [\(6\)](#) involve  $w_k$ ,  $w_s$ , and the temperature differences across the layers. For the numerical implementation of these terms, readers are referred to [McCreary and Kundu \(1989\)](#).

The model domain includes all longitudes and extends latitudinally from 65°S to 35°N. The model has realistic coastline geometry that is determined by the 200-m depth contour. To adequately resolve the detailed coastline features surrounding the Indonesian archipelago, the model grid has the finest resolution of  $1/6^\circ$  in latitude and  $1/6^\circ$  in longitude in the region from 8°S to 8°N, 118° to 130°E. The grid size increases gradually away from this focus region to  $1^\circ$  in latitude and  $1^\circ$  in longitude.

[Equations \(1\)–\(6\)](#) are solved in finite difference form using the energy-conserving scheme proposed by [Sadourney \(1975\)](#). The Arakawa C-grid is used in defining the staggered positions for the dependent variables  $u$ ,  $\mathbf{u}$ , and  $h$  ([Arakawa and Lamb 1977](#)). Temperatures are defined at the point of  $h$ . Along the model's open ocean boundaries (in the North Pacific and North Atlantic along 35°N), no-normal flow and free-slip conditions are used. No-normal-flow and non-slip conditions are used along the coast and marginal seas (depth <200 m). The horizontal eddy viscosity/diffusivity coefficient is  $400 \text{ m}^2 \text{ s}^{-1}$  in the model's tropical region. The  $A_h$  ( $K_h$ ) value increases gradually to  $2500 \text{ m}^2 \text{ s}^{-1}$  at higher latitudes where the model grid size is coarse. Values for the other parameters used in the model simulation are listed in [Table 1](#).

The model ocean, which is initially at rest, is spun up by the monthly, climatological wind of [Hellerman and Rosenstein \(1983\)](#). For the surface thermal forcing, we followed the formulation proposed by [Barnier et al. \(1995\)](#):

$$\frac{Q}{\rho_o c_p h_m} = \frac{Q^{\text{clim}}}{\rho_o c_p h_m} + \frac{1}{R_T} (T^{\text{clim}} - T_m); \quad (7)$$

namely, it contains a climatological heat flux ( $Q^{\text{clim}}$ ) term and a correction term proportional to the difference between the

climatological SST ( $T^{\text{clim}}$ ) and the model predicted mixed layer temperature. In [Eq. \(7\)](#),  $R_T$  is the relaxation timescale with a value of 40 days. For the  $Q^{\text{clim}}$  and  $T^{\text{clim}}$  fields used in the model simulation, we adopted the COADS monthly climatological dataset of [DaSilva et al. \(1994\)](#).

In addition to the base model case described above, we carried out other model experiments in which we either changed the model's coastline configuration or forced the model ocean using the daily ECMWF surface wind data. These additional experiments are conducted in order to test hypotheses on the generation mechanisms of the 40–60 day signals found around the Indonesian archipelago. The details of these experiments will be described in [sections 4](#) and [5](#). For all the model cases, we integrated the governing equations till the temperature and flow fields reached statistical equilibrium. Thereafter, an additional 4-yr integration was carried out and the results from these 4 years are used in the following analyses.

### 3. Results of the base model case

In this section, we examine the results of the base model case forced by the monthly climatological surface wind and heat flux data. The focus will be on both seasonal and intraseasonal signals in regions surrounding the Indonesian archipelago. A discussion of the seasonal variability helps validate model results through comparison with existing studies; it also provides a context for our following investigation of the intraseasonal signals.

#### *a. Mean state and seasonal variability*

[Figure 4](#) shows the annually averaged upper-layer flow field derived from the base model case in the region surrounding the Indonesian archipelago. The flow pattern agrees well with that derived from observations (e.g., [Lukas et al. 1991](#)) and it is also similar to the mean flow patterns obtained in past modeling studies (e.g., [Kindle et al. 1989](#); [Inoue and Welsh 1993](#); [Masumoto and Yamagata 1993](#); [Miyama et al. 1995](#)). Briefly, the Pacific-origin waters move to the Indian Ocean following two major routes. The “western route” begins as a southwestward branch of the Mindanao Current, which bifurcates at the entrance of the Celebes Sea and passes through the Makassar Strait. One part enters the Indian Ocean through the Lombok Strait; the other part veers eastward through the Flores Sea to reach the Banda Sea. In the Banda Sea, part of this flow recirculates back northward to merge with the North Equatorial Countercurrent (NECC) east of the Celebes Sea. The remaining part of the “western route” flow continues eastward in the Banda Sea and is joined by the weak “eastern route” flow coming directly from the north through the Halmahera Sea. Together, they enter the Indian Ocean through the Ombai Strait and the Timor Passage (see [Fig. 1](#)).

[Figure 5](#) shows the time series of the modeled transport through the Lombok Strait, the Ombai Strait, and the Timor Passage. The total ITF transport through these three straits is given in [Fig. 5d](#). The mean ITF transport from our model is 6.9 Sv, which is in the mid range of the previous indirect estimates (see [Table 1](#) of [Godfrey 1996](#)). This value for the mean ITF is close to the recent estimate of 7 Sv by [Meyers et al. \(1995\)](#) based on the long-term XBT measurements between Java and Australia. The annual cycle of the modeled ITF has a minimum transport in January/February and a broad maximum transport from June to November. The phase of this annual cycle agrees well with the annual cycle of the ITF transport inferred from the sea level difference between Davao and Darwin by [Wyrcki \(1987\)](#).

Among the three straits contributing to the ITF, [Fig. 5a](#) shows that Lombok Strait carries a mean transport of 3.0 Sv, which is 43% of the mean total ITF. This transport value is somewhat larger than 1.7 Sv estimated by [Murray and Arief \(1988\)](#) based on in situ current meter measurements. Their measured ITF transport through Lombok Strait fluctuated from near zero in February to about 5 Sv in August, a seasonal signal also evident in the model result of [Fig. 5a](#). The Ombai Strait carries a mean transport of 1.1 Sv (16% of the mean total ITF) and its annual cycle is similar in phase with that in Lombok Strait. The Timor Passage in our model carries a mean transport of 2.8 Sv; this value is close to 3.5 Sv derived by [Cresswell et al. \(1993\)](#) for the upper 350 m layer transport in the Timor Passage based on Pegasus and ADCP measurements.

In the India Ocean south of the Indonesian archipelago, the combined ITF outflows from the three straits are incorporated into the South Equatorial Current (SEC), which flows westward in the zonal band between 9° and 14°S (see [Fig. 4](#)). The annual cycle of the modeled SEC has a maximum transport in August/September and a minimum in April ([Fig. 6a](#)); it agrees favorably with the SEC's annual cycle observed by [Meyers et al. \(1995\)](#) from the repeat XBT measurements between Java and Australia. Notice that a weak eastward flowing South Java Current exists along the southern coast of Java in the mean flow field of [Fig. 4](#). The modeled South Java Current, defined here as a zonal flow between 9°S and the Java coast, has a clear semiannual variation with maximum eastward flow appearing in spring and fall ([Fig. 6b](#)). This semiannual signal of the South Java Current is consistent with the observations reported by [Clarke and Liu \(1993\)](#) and [Meyers et al. \(1995\)](#).

Finally, the mean flow pattern in the low-latitude western Pacific is well established from observations (e.g., [Lukas et al. 1991](#); [Tsuchiya et al. 1990](#)). The model result shown in [Fig. 4](#) is again in good agreement with these studies. Major

circulation features here include bifurcation of the North Equatorial Current (NEC) at 14°N along the Mindanao coast to form the Kuroshio and the Mindanao Current, confluence of the Mindanao Current and the South Equatorial Current to form the eastward flowing North Equatorial Countercurrent (NECC), and the presence of the quasi-permanent Mindanao and Halmahera eddies (centered at 7°N, 130°E and 3°N, 130.5°E, respectively). As it is not the focus of this study, the detailed seasonal variability of these circulation features will not be presented here.

### *b. Intraseasonal variability*

Given the newly available current meter data shown in [Fig. 2](#), it is interesting to first look into the modeled velocity field at the same geographical location (4.0°N, 127.5°E). [Figure 7a](#) shows the time series of the meridional velocity obtained in the base model case. Here, the  $v$  component of the velocity is selected because it showed the clearest intraseasonal signal in the observations ([Watanabe et al. 1997](#)). [Figure 7b](#) compares the power spectrum from the modeled time series ([Fig. 7a](#)) with that from the observations. While the rms amplitude of the observed  $v$  velocity is about one order of magnitude smaller than the model's (recall that the observation was made at the 350-m depth, whereas [Fig. 7a](#) represents the averaged  $v$  velocity in the upper 270-m layer), the dominance of the intraseasonal signals with periods around 50 days is obvious in both model and observations.

Since the climatological monthly wind data are used to force the base model, the direct model response to the wind forcing is limited to timescales of 2 months and longer. The result of [Fig. 7](#), thus, suggests that the internal dynamics of the ocean *alone* can possibly explain the intraseasonal signals observed at the Pacific entrance of the Indonesian seas ([Fig. 2](#)). This result per se, however, cannot be used to dismiss the possible roles played by the external high-frequency wind forcing. To do so requires a comparison with a model run that is forced by surface wind including high frequency signals. Another question related to [Fig. 7](#) is what ocean dynamics is responsible for determining the predominant timescale of the intraseasonal signals. In other words, why is the 50-day oscillation being preferentially selected near the entrance of the Celebes Sea? These two questions will be addressed in [section 4](#).

Notice that areas with significant intraseasonal signals are not only confined to the Celebes Sea. As presented in [Fig. 8](#), intraseasonal variability with the eddy kinetic energy ratio greater than 5% can be found in most of the low-latitude western Pacific Ocean and the Indonesian seas. Here, the energy ratio is defined as the eddy kinetic energy in the 30–60 day frequency band versus that over the whole frequency band (i.e., the total eddy kinetic energy). Particularly large intraseasonal signals, with the eddy kinetic energy ratio greater than 25%, are present in three areas: the Celebes Sea, the Banda Sea, and the area of the Mindanao eddy. One interesting aspect revealed by [Fig. 8](#) is that a part of the intraseasonal signals in the Indonesian seas is able to “leak” southward along the northeast coast of Australia via baroclinic coastal Kelvin waves. A manifestation of this leakage can be also seen in [Fig. 5](#) in which high-frequency signals are apparent in the time series of the transport through Timor Passage. Details of the intraseasonal signals in Timor Passage will be discussed in [section 5b](#).

In the eastern Indian Ocean away from the Australia coast, [Fig. 8](#) shows that the intraseasonal signals are almost nonexistent. This base model result is quite different from available observations. For example, [Figs. 9a and 9b](#) show the sea level time series measured at the tide gauge stations at Benoa (8.7°S, 115.2°E) near the Lombok Strait and at Christmas Island (10.4°S, 105.7°E). As indicated in [Fig. 9c](#), intraseasonal signals with a dominant spectral peak around 50–60 days and a secondary peak around 85 days are present at both of these locations. Clearly, these intraseasonal signals and those described recently by [Bray et al. \(1997\)](#) are induced by mechanisms that are missing from our base model case. An in-depth examination into the intraseasonal variability in the outflow region of the ITF will be conducted in [section 5](#).

## **4. Intraseasonal variability in the low-latitude western Pacific**

The base model result of [section 3](#) revealed that the internal dynamics of the ocean alone can generate significant intraseasonal variability in the low-latitude western Pacific Ocean and within the Indonesian seas. A question arising naturally is to what extent the high-frequency wind forcing, which is absent in the [Hellerman and Rosenstein \(1983\)](#) climatological wind data, can modify the intraseasonal signals modeled in these regions. To address this question, we carried out an additional model experiment in which we forced the model ocean by daily averaged, 1000-mb wind data of the European Centre for Medium-Range Weather Forecasts (ECMWF). For this “daily model case,” we used the base model result as initial condition and extended the model integration over a 10-yr period using the available wind data from 1980 to 1989. The ensuing discussions are based on the model output from 1985 to 1989.

[Figure 10](#) shows the time series and power spectrum of the meridional velocity at the mooring site of the Celebes Sea from the daily model case. Not surprisingly, the energy level in the frequency band from 30 to 100 days is generally higher in the daily model case than in the base case (cf. [Fig. 7](#)). Like in the base model case, however, the dominance of the near-50-day oscillation is again obvious. It is interesting to note that a secondary energy peak exists with a wave period of about 100 days in the power spectrum of the daily model result. A similar energy peak is discernible in the power spectrum of the observed velocity time series ([Fig. 2](#)), although the observed 100-day signals appear to have much less energy

compared to the 50-day signals than in the daily model result. As far as the dominant 50-day signals are concerned, the comparison between the base and daily model results clearly suggests that the high-frequency surface wind forcing is not essential. In other words, the intraseasonal signals presented in Fig. 2 are determined by internal ocean dynamics.

### a. Dynamic role of the Celebes Sea basin

To explore the ocean dynamics important for the observed intraseasonal signals, it is helpful to first examine the detailed circulation patterns in the Celebes Sea. Figure 11 shows a sequence of snapshots of the upper-layer thickness field from the base model output at 10-day intervals. Figure 11a shows a fully developed cyclonic eddy close to break off from the Mindanao Current. In Fig. 11b, this cyclonic eddy breaks off from the Mindanao Current and has a diameter of  $d = 450$  km. Based on conservation of potential vorticity, Hurlburt and Thompson (1980) showed that the size of a cutoff eddy from a boundary current is given by  $d = 2(V_c/\beta)^{1/2}$ , where  $V_c$  is the core speed of the boundary current and  $\beta$  is the  $y$  derivative of the Coriolis parameter. With  $V_c = 1.2$  m s<sup>-1</sup> estimated from the modeled Mindanao Current and  $\beta = 2.3 \times 10^{-11}$  s<sup>-1</sup> m<sup>-1</sup>, the theory predicts  $d = 457$  km, a value matching well with the size of the modeled cutoff eddy shown in Fig. 11b. In Fig. 11c, this cutoff eddy drifts westward and subsequently disappears from the Celebes Sea after it reaches the western boundary (Fig. 11d). Meanwhile a new cyclonic eddy begins to form in the Mindanao Current. This new eddy reaches a breaking-off state similar to the previous eddy shown in Fig. 11a with a time separation of 50 days (Fig. 11f).

Figure 12 shows the  $x$ - $t$  diagram of the modeled upper-layer thickness anomalies along the center latitude (4°N) of the Celebes Sea. It indicates that the eddy shedding event depicted in Fig. 11 takes place regularly about every 50 days. The westward propagating speed of the cutoff eddies based on the anomaly slopes shown in Fig. 12 is about 0.21 m s<sup>-1</sup>. This propagating speed can be compared with the phase speed of dispersive baroclinic Rossby waves:

$$c_{px} = -\frac{\beta}{k^2 + l^2 + f^2/g'h}, \quad (8)$$

with  $k = l = \pi/d$ . Using  $d = 450$  km,  $g'h = 9.1$  m<sup>2</sup> s<sup>-2</sup>, and  $f = 1.02 \times 10^{-5}$  s<sup>-1</sup>, we have  $c_{px} = -0.21$  m s<sup>-1</sup>, suggesting the westward propagation of the cutoff eddies is constrained by the baroclinic Rossby wave dynamics. That the cutoff eddies tend to propagate westward at the phase speed of dispersive baroclinic Rossby waves is also true for the Loop Current eddies in the Gulf of Mexico (see Hurlburt and Thompson 1980). Notice that the presence of the cyclonic eddies cut off from the Mindanao Current can be seen in some of the surface drifter trajectories observed in the Celebes Sea. As depicted in Fig. 2 of Lukas et al. (1991), of the four drifters that entered the Celebes Sea, two looped cyclonically before entering Makassar Strait, one showed sign of cyclonic looping (but demised prematurely), and one passed through the Celebes Sea without looping.

While the eddy shedding events are clearly responsible for the near-50-day signals in the Celebes Sea, we emphasize that the basin size of the Celebes Sea is another critical parameter for the intraseasonal signals in the low-latitude Pacific Ocean and the Indonesian seas. For a rectangular basin with a zonal length of  $L_x$  and a meridional length of  $L_y$ , the intrinsic frequency for the basin Rossby modes is given by

$$\omega = \frac{\beta}{2} \left( \frac{n^2 \pi^2}{L_x^2} + \frac{m^2 \pi^2}{L_y^2} + \frac{f^2}{g'h} \right)^{-1/2}, \quad (9)$$

where  $n$  and  $m$  are mode numbers in the  $x$  and  $y$  directions (see LeBlond and Mysak 1978, 299–302). For values appropriate for the Celebes Sea,  $L_x = 720$  km,  $L_y = 500$  km,  $g'h = 9.1$  m<sup>2</sup> s<sup>-2</sup>,  $f = 1.02 \times 10^{-5}$  s<sup>-1</sup>, and  $\beta = 2.3 \times 10^{-11}$  s<sup>-1</sup> m<sup>-1</sup>, the gravest basin Rossby mode ( $n = m = 1$ ) has an intrinsic wave period of 52.8 days. This close match between the period of the eddy shedding from the Mindanao Current and the intrinsic wave period of the Celebes Sea basin suggests that resonance could have played an important role in the results presented above. To test this hypothesis, we conducted two model experiments in which we artificially altered the basin size of the Celebes Sea, while keeping all other conditions the same as the base model case. In the “large CS case,” we enlarged the basin size by shifting Minahassa Peninsula southward by 2.0° latitude (see the checkered block in Fig. 13b), whereas in the “small CS case,” we reduced the basin size of the Celebes Sea by shifting Minahassa Peninsula northward by 1.5° latitude (see the checkered block in Fig. 13c). This effectively shifts the intrinsic wave period of the Celebes Sea to 43.7 days in the large SC case and to 68.6 days in the small CS case, respectively.

Figure 13b and 13c show the 30–60 day bandpassed eddy kinetic energy distributions from the large and small CS cases. Their difference from the base model case shown in Fig. 13a is striking. In the large CS case, not only is the

intraseasonal eddy kinetic energy peak in the Celebes Sea no longer present, but also the offshore intraseasonal energy peak associated with the Mindanao eddy and the NECC is greatly reduced. This drastic reduction in intraseasonal eddy kinetic energy in the large CS case is due to the fact that the Mindanao Current in this case intrudes into the Celebes Sea and forms a relatively stable cyclonic circulation that occupies the entire enlarged Celebes Sea (not shown). In the small CS case, on the other hand, the intrusion of the Mindanao Current into the Celebes Sea is dynamically prohibited, as the Celebes Sea width in this case (335 km) is narrower than the cutoff eddy diameter (450 km). The intraseasonal eddy kinetic energy associated with the Mindanao eddy and the NECC is slightly higher in the small CS case than in the base model case. In short, the model result of [Fig. 13](#) demonstrates that the intense 50-day oscillation observed at the entrance of the Celebes Sea ([Fig. 2](#)) is a result of Rossby wave resonance, in which the frequency of cyclonic eddy shedding by the retroflecting Mindanao Current matches that of the gravest Rossby mode in the Celebes Sea basin.

### *b. Impact of Celebes Sea–originated 50-day oscillations*

One consequence of the Rossby wave resonance in the Celebes Sea is that the western route ITF is being periodically “perturbed” at the 50-day timescale. This is obvious in [Fig. 14](#), which shows the throughflow transport through the Makassar Strait from the base model run. It is interesting to note that the influence of this 50-day oscillation reaches the Banda Sea (a region where the modeled intraseasonal eddy kinetic energy ratio is relatively high; see [Fig. 8](#)) and the Timor Passage, but does not impact the Lombok and Ombai Straits significantly (see [Figs. 5a–c](#)). This may appear paradoxical as both the Lombok and Ombai Straits are located geographically closer to the Makassar Strait than are the Banda Sea and the Timor Passage. To clarify this point, we conducted a simple model experiment, in which we locally excited 50-day oscillations in the Celebes Sea by imposing an oscillatory surface wind in the Celebes Sea basin. [Figure 15a](#) shows the distribution of the upper-layer thickness variance derived from this idealized model run. Following the sequence of the model output reveals that the Celebes Sea–originated 50-day oscillation affects the surrounding waters by way of coastal Kelvin waves. After passing through the Makassar Strait, the intraseasonal Kelvin wave signal follows the coast of Sulawesi, loops around the Banda Sea, and part of it leaks into the Indian Ocean through the Timor Passage along the shallow continental slope west of Australia.

Examining the flow transport through the various straits in the Indonesian seas ([Fig. 15b](#)) shows that the transport peak in the Timor Passage lags about 12 days behind that in the Makassar Strait, the time it takes for the coastal Kelvin waves to travel from the Makassar Strait to the Timor Passage. The amplitude of the flow through the Timor Passage is about 30% of that through the Makassar Strait. As the coastal Kelvin waves loop around the Banda Sea, a small portion of the 50-day signal also reaches the Ombai Strait. The wave amplitude there, however, is further attenuated as compared to the amplitude in the Timor Passage. Little wave energy appears to reach the Lombok Strait, which is located farther to the west.

In concluding this section, we note that the intraseasonal signals originating in the low-latitude western Pacific boundary affect the ITF preferentially through the Timor Passage. For the observed throughflow fluctuations in the Timor Passage, however, it will become clear in [section 5b](#) that the intraseasonal along-archipelago wind in the eastern Indian Ocean plays a more important role than do the remote wave signals from the Celebes Sea.

## **5. Intraseasonal variability in the eastern Indian Ocean and the Indonesian seas**

On the Indian Ocean side of the Indonesian seas, away from the Australia coast, the base model result of [Fig. 8](#) shows that the intraseasonal signals are essentially nonexistent. This suggests that the intraseasonal signals observed in this region, such as those presented in [Fig. 9](#), must be induced by high-frequency winds missing in the climatological wind dataset. Indeed, forcing the model ocean using the daily ECMWF wind data (the daily model case) reveals that the eddy kinetic energy ratio in the intraseasonal frequency band increases significantly in the eastern Indian Ocean ([Fig. 16](#)). The eddy kinetic energy ratio along the Java coast, for example, increased from <0.5% in the base model case of [Fig. 8](#) to 15%–20% in [Fig. 16](#).

### *a. Local versus remote wind forcing*

A detailed comparison can be made at Benoa where observed sea level data are available (see [Fig. 9](#)). [Figure 17a](#) shows a 3-yr time series of the upper-layer thickness anomalies at Benoa from the daily model run. In the intraseasonal frequency band, the modeled time series is dominated by oscillations with periods around 50 and 85 days (the solid line in [Fig. 17c](#)), resembling the characteristics of the observed sea level signals. Note that the modeled energy peak around 85 days is comparable in magnitude with the 50-day peak, whereas it is weaker than the 50-day peak in the observations. While they are clearly wind-forced, these intraseasonal signals can dynamically be driven either by local winds along the Java coast or by the remote wind along the equatorial Indian Ocean. Indeed, several investigators in the past have suggested the remote equatorial wind forcing is responsible for exciting the intraseasonal oscillations in the ITF outflow regions (e.g., [Arief and Murray 1996](#); [Molcard et al. 1996](#)).



To evaluate the relative importance of the local wind versus the remote wind in forcing intraseasonal signals along the Java coast, we carried out an additional model experiment in which we forced the model in the eastern Indian Ocean (east of 100°E) and the Indonesian seas by the daily ECMWF wind data and the rest of the world ocean by the climatological [Hellerman and Rosenstein \(1983\)](#) wind data. This model experiment effectively removes all influences of the intraseasonal wind forcing along the equatorial Indian Ocean and is referred to as the “local model case” below. The solid line in [Fig. 17b](#) shows the time series of the upper-layer thickness anomalies at Benoa obtained from this local model run. Compared to [Fig. 17a](#), the amplitude of the intraseasonal signals in this time series is greatly reduced. Also, the 50-day spectral peak computed from this time series is no longer as distinctive as that from the daily model result (see [Fig. 17c](#)). While the comparison between the local model time series and the base model time series (the dashed line in [Fig. 17b](#)) does indicate that the local wind along the Java coast induces the intraseasonal signals to some extent, our above model results indicate that it is the remote wind forcing along the equatorial Indian Ocean that determines the energy level of the intraseasonal signals along the Java coast.

Given the importance of the remote equatorial wind in exciting the intraseasonal signals along the Java coast, we next examined the characteristics of the surface wind along the equatorial Indian Ocean. [Figure 18](#) shows the power spectra of the zonal wind stress along the equator of the Indian Ocean in the intraseasonal frequency band. Not surprisingly, spectral peaks indeed exist around 50 and 85 days in the zonal wind data, which correspond to the intraseasonal spectral peaks of the oceanic response at Benoa (see [Fig. 9c](#)). Notice that the largest intraseasonal wind signals are located in the central Indian Ocean from 70° to 90°E and that the 50- and 85-day signals are more energetic in the zonal component of the wind stress data than in the meridional component (not shown). In the segments of 50°–60°E and 90°–100°E near the equatorial land boundaries, the wind stress data show no clear spectral peaks in bands with wave periods longer than 40 days.

### *b. Intraseasonal signals in through-strait flows*

As the surface wind in the central equatorial Indian Ocean fluctuates intraseasonally, it generates eastward propagating equatorial Kelvin waves. Upon reaching the coast of Sumatra, these equatorial waves continue to move poleward in the form of coastal Kelvin waves. The intraseasonal signals at Benoa as shown in [Fig. 17a](#) are largely due to the passage of these coastal Kelvin waves. Notice that the Lombok Strait exists next to Benoa and is the first deep strait a poleward-moving coastal Kelvin wave would encounter along the Indonesian archipelago. Does this coastline gap of the Lombok Strait interrupt the poleward movement of the remotely forced coastal Kelvin waves? Interestingly, unlike the intraseasonal signals at Benoa, the moored current meter data obtained at the Timor Passage by Molcard et al. (see [Fig. 3](#)) revealed no clear spectral peaks around the 50- and 85-day periods. This suggests that the Lombok Strait may play an important role in preventing the remotely forced coastal Kelvin waves from effectively influencing the downstream poleward regions.

To quantitatively assess the influence of the remotely forced coastal Kelvin waves upon the variability in the downstream Ombai and Timor Straits, we carried out a model experiment similar to that presented in [Fig. 15](#) except, in this case, we imposed the oscillatory wind forcing in a localized area centered on the equator and 90°E. [Figure 19a](#) shows the distribution of the upper-layer thickness variance derived from this model experiment; the time series of the transport through the four straits of our interest are presented in [Fig. 19b](#). A close look at the paths of the Kelvin wave signals (not shown here) reveals that as the poleward propagating coastal Kelvin waves reach the gap of the Lombok Strait,<sup>1</sup> the majority of the wave signals turn northward entering the Makassar Strait. As these waves move equatorward, their horizontal scale increases due to decreasing  $f$ . In the narrow Makassar Strait, the coastal Kelvin waves become wide enough to reach the west coast of Sulawesi and a portion of the wave signals is able to propagate cyclonically around the coast of Sulawesi, circulate the Banda Sea, and eventually reach the Timor Strait. Because of this indirect route, the Ombai Strait is now on the downstream side of the Timor Passage, and this is why the wave amplitude detected in the Ombai Strait in [Fig. 19b](#) is smaller than that in the Timor Passage. For both of these two straits, [Fig. 19b](#) demonstrates that the influence from the coastal Kelvin waves remotely forced in the equatorial Indian Ocean is small.

The result from this idealized model experiment also provides a base for understanding the intraseasonal ITF variability obtained in the daily model case. [Figure 20](#) shows the transport time series through the Lombok, Ombai, Timor, and Makassar Straits from the daily model run. As indicated in [Fig. 21a](#), the characteristics of the intraseasonal signals in the Lombok and Makassar Straits are similar, both having dominant spectral peaks around 50 and 85 days. In light of the above discussion, this is understandable because the 50- and 85-day signals are remotely excited in the central equatorial Indian Ocean and they can intrude largely unobstructedly into the Lombok Strait and reach the Makassar Strait. That the energy levels of the 50- and 85-day signals in [Fig. 21a](#) are higher in the Makassar Strait than in the Lombok Strait is due to the additional, intraseasonal signal input from the Celebes Sea (see the detailed discussion in [section 4](#)). Recall that the Celebes Sea-originated intraseasonal signals have little impact upon the transport in the Lombok Strait.

The characteristics of the intraseasonal signals in the Timor Passage ([Fig. 21b](#)) are quite different from those in the Lombok and Makassar Straits.<sup>2</sup> In the Timor Passage, the 50-day oscillations are no longer the dominant intraseasonal signals. Instead, a broad 30–35-day spectral peak becomes apparent. Note that this spectral peak around 30–35 days also

exists in the in situ current meter data from the Timor Passage (see [Fig. 3](#) and [Molcard et al. 1994](#)). Like in the Lombok and Makassar Straits, an 85-day spectral peak appears in [Fig. 21b](#). The origin for the 85-day signals in the Timor Passage, however, is different from that in the Lombok Strait. The latter, as we discussed in [section 5a](#), comes from the surface zonal wind fluctuations in the central equatorial Indian Ocean. For the Timor Passage, both of the 85-day signals and the shorter-period, 30–35-day signals are induced by local wind. This is evident if we look into the zonal wind stress data along the Indonesian coast from 100° to 125°E ([Fig. 22](#)). Along the Sumatra coast of 100°–105°E and the Java coast of 105°–110°E, the wind stress data exhibits a spectral peak around 50 days. East of 110°E the 50-day spectral peak weakens and is replaced by the dual spectral peaks centered on 85 and 35 days. As one moves eastward toward the Timor Passage at 125°E, these two spectral peaks become more prominent. Notice that the 85-day spectral peak is absent in the observed alongchannel flow in the Timor Passage (see [Fig. 3b](#)). This could be due to the short length of the mooring record (about 330 days) or to the interannual changes in the surface wind's intraseasonal characteristics.

One available mooring record that overlaps with the simulation period of the daily model case (1980–89) is that of [Murray and Arief \(1988\)](#) from the Lombok Strait. The solid line in [Fig. 23](#) shows the time series of the meridional flow observed by Murray and Arief at a 35-m depth of the Lombok Strait. The dashed line in [Fig. 23](#) shows the flow transport through the Lombok Strait from the daily model case. The agreement between the two time series is favorable with the modeled through-channel flow capturing most of the observed intraseasonal signals. The cross-correlation coefficient between the two time series is 0.70; it is significant at the 99% confidence level with the degrees of freedom for the time series estimated at 20. This favorable comparison between the model and the observation is encouraging as it lends credibility to the physical explanations provided in this study for the observed intraseasonal signals.

### *c. Intraseasonal signals in the Indonesian–Australian basin*

In the Indonesian–Australian basin away from the Java coast, [Bray et al. \(1997\)](#) observed strong 60-day sea surface height fluctuations associated with the eddies and meanders of the South Equatorial Current. As shown by Bray et al., these fluctuations are well captured by the sea level measurement at Christmas Island (10.4°S, 105.7°E), which is located near the northern edge of the SEC. The intraseasonal signals in the SEC of our daily model simulation are relatively weak. A look at the modeled sea level time series at Christmas Island ([Fig. 24](#)) reveals that while the 60- and 90-day spectral peaks are discernible due to the intraseasonal wind forcing, their amplitudes are an order of magnitude smaller than those from the tide gauge measurement (cf. [Fig. 9c](#)). We speculate that this discrepancy is attributable to the deficiency of our present 1½-layer model that disallows baroclinic instability to develop in the SEC. Questions such as what determines the timescale of the intraseasonal changes of the SEC and whether the regional intraseasonal wind forcing contributes to the selection of this timescale need to be addressed in future studies.

## 6. Summary

Recent long-term current meter observations from the low-latitude Pacific western boundary and from around the Indonesian archipelago regions revealed the ubiquitous presence of flow fluctuations with intraseasonal timescales. Theoretically, intraseasonal fluctuations in the upper-ocean circulation can be excited through several dynamic processes: direct wind forcing, wind forcing in remote areas via waveguide, mean flow instability, and resonance due to coastline geometry. The objective of this study is to clarify the dynamic processes underlying the observed intraseasonal signals at different locations around the Indonesian seas.

To achieve this, we used a fine-resolution, 1½-layer reduced-gravity model with the Kraus and Turner mixed layer dynamics embedded. The model simulated well both the mean circulation and the seasonal/intraseasonal signals observed around the Indonesian seas. Our model experiments ranged from simple cases, where either climatological or idealized surface wind forcing was adopted, to a more realistic case in which we used the daily ECMWF surface wind data. Given the complex coastline geometry in the Indonesian seas and the richness in the surface wind variability, these model experiments with various levels of complexity helped test hypotheses and shed light on the physics essential for the observed intraseasonal signals.

At the Pacific entrance of the Celebes Sea, our study showed that the energetic 50-day oscillations detected by a recent current meter mooring observation were a result of Rossby wave resonance in the Celebes Sea basin. As the Mindanao Current retroflects eastward offshore of Mindanao, it sheds cyclonic eddies into the semi-enclosed Celebes Sea. The eddy shedding period, which is determined by the length scale and the westward translating speed of the cutoff eddies, is about 50 days and matches closely the gravest Rossby mode of the Celebes Sea basin. This match amplifies the 50-day signals in the Celebes Sea and its effect further influences the ITF in the Makassar Strait.

Intraseasonal signals along the Sumatra/Java coasts in the eastern Indian Ocean are dominated by oscillations with wave periods of 50 days and 85 days. These signals have been observed both by tide gauges along the Sumatra/Java coasts and by current meter moorings in the Lombok Strait. The origin of these wave signals can be traced back to the central equatorial Indian Ocean where the surface zonal wind fluctuates intraseasonally with the same wave periods of 50 and 85 days. When

the coastal Kelvin waves that are remotely excited as equatorial Kelvin waves in the central Indian Ocean reach the Lombok Strait, most of the wave signals do not continue poleward along the archipelago coast. Rather, these waves enter the Makassar Strait and affect areas in the Banda Sea and around the coast of Sulawesi. Because of this in-land route, the 50- and 85-day signals of the equatorial Indian Ocean–origin do not have a significant effect on the throughflow fluctuations in the Timor and Ombai Straits.

Intraseasonal signals observed in the surface layer of the Timor Passage are dominated by oscillations with wave periods of 30–35 days. Our model result suggested that a second spectral peak with an 85-day wave period existed for the time period from 1985 to 1989 as well. Along the Indonesian archipelago coast between 115° and 125°E, the surface zonal winds have dominant spectral peaks around 35 and 85 days. It is these regional wind forcings that are responsible for the observed and modeled transport fluctuations in the Timor Passage. Notice that although the Timor Passage is in the pathway of the coastal Kelvin waves originating in the upstream Celebes Sea or along the Sumatra/Java coasts, the influence from these waves appears to be small in comparison with the local-wind-induced intraseasonal signals.

Finally, this study has been motivated by several recent observational studies around the Indonesian archipelago regions. While the in situ data are still limited from these regions, observational efforts are presently being made by scientists from various countries. We believe that future modeling studies, when combined with new observational results, will be useful in improving our understanding of the intraseasonal variability in this important part of the World Ocean.

### Acknowledgments

We thank Akio Ishida, Roger Lukas, Toru Miyama, and Jim Potemra for their interest and discussions during the course of this study. Jackson Chong, Stuart Godfrey, Steve Murray, Susan Wijffels, and an anonymous reviewer carefully read an earlier version of the manuscript and provided many helpful comments. The in situ velocity time series presented in [Fig. 3a](#) was provided to us by Robert Molcard, the ECMWF daily wind data by NCAR, and the in situ sea level data by the Sea Level Center at University of Hawaii. We are grateful to the Maui High Performance Computer Center for contributing the computer time used in our modeling work. B.Q. and M.M. were supported by NOAA through the Wyrтки Climate Research Center at the University of Hawaii (Cooperative Agreement NA67RJ0154).

---

### REFERENCES

- Arakawa, A., and V. R. Lamb, 1977: Computational design of the basic dynamical processes of the UCLA General Circulation Model. *Method Comput. Phys.*, **17**, 173–265..
- Arief, D., and S. P. Murray, 1996: Low-frequency fluctuations in the Indonesian throughflow through Lombok Strait. *J. Geophys. Res.*, **101**, 12 455–12 464..
- Barnier, B., L. Siefridt, and P. Marchesiello, 1995: Thermal forcing for a global ocean circulation model using a three-year climatology of ECMWF analyses. *J. Mar. Sys.*, **6**, 363–380..
- Bray, N. A., S. E. Wijffels, J. C. Chong, M. Fieux, S. Hautala, G. Meyers, and W. M. L. Morawitz, 1997: Characteristics of the Indo-Pacific throughflow in the eastern Indian Ocean. *Geophys. Res. Lett.*, **24**, 2569–2572..
- Broecker, W. S., 1991: The great ocean conveyor. *Oceanography*, **4**, 79–89..
- Clarke, A. J., and X. Liu, 1993: Observations and dynamics of semiannual and annual sea levels near the eastern equatorial Indian Ocean boundary. *J. Phys. Oceanogr.*, **23**, 386–399.. [Find this article online](#)
- , and —, 1994: Interannual sea level in the northern and eastern Indian Ocean. *J. Phys. Oceanogr.*, **24**, 1224–1235.. [Find this article online](#)
- Cresswell, G., A. Frische, J. Peterson, and D. Quadfasel, 1993: Circulation in the Timor Sea. *J. Geophys. Res.*, **98**, 14 379–14 389..
- Da Silva, A. M., C. C. Young, and S. Levitus, 1994: *Atlas of Surface Marine Data 1994*, Vol. 1: *Algorithms and Procedures*, NOAA Atlas NESDIS 6. NOAA, U.S. Dept. of Commerce, Washington, D.C., 83 pp..
- Ffield, A., and A. L. Gordon, 1992: Vertical mixing in the Indonesian thermocline. *J. Phys. Oceanogr.*, **22**, 184–195.. [Find this article online](#)
- , and —, 1996: Tidal mixing signatures in the Indonesian seas. *J. Phys. Oceanogr.*, **26**, 1924–1937.. [Find this article online](#)
- Godfrey, J. S., 1996: The effect of the Indonesian throughflow on ocean circulation and heat exchange with the atmosphere: A review. *J. Geophys. Res.*, **101**, 12 217–12 237..

- , and T. J. Golding, 1981: The Sverdrup relation in the Indian Ocean, and the effect of Pacific–Indian Ocean throughflow on Indian Ocean circulation and on the East Australian Current. *J. Phys. Oceanogr.*, **11**, 771–779.. [Find this article online](#)
- Gordon, A. L., 1986: Inter-ocean exchange of thermocline water. *J. Geophys. Res.*, **91**, 5037–5046..
- Hellerman, S., and M. Rosenstein, 1983: Normal monthly wind stress over the world ocean with error estimates. *J. Phys. Oceanogr.*, **13**, 1093–1104.. [Find this article online](#)
- Hurlburt, H. E., and J. D. Thompson, 1980: A numerical study of loop current intrusions and eddy shedding. *J. Phys. Oceanogr.*, **10**, 1611–1651.. [Find this article online](#)
- , J. C. Kindle, E. J. Metzger, and A. J. Wallcraft, 1989: Results from a global model in the western tropical Pacific. *Proc. Western Pacific Int. Meeting and Workshop on TOGA COARE*, Noumea, New Caledonia, Centre ORSTOM de Noumea, 343–354..
- Inoue, M., and S. E. Welsh, 1993: Modeling seasonal variability in the wind-driven upper-layer circulation in the Indo–Pacific region. *J. Phys. Oceanogr.*, **23**, 1411–1436.. [Find this article online](#)
- Kashino, Y., H. Watanabe, B. Herunadi, M. Aoyama, and D. Hartoyo, 1999: Current variability at the Pacific entrance of the Indonesian Throughflow. *J. Geophys. Res.*, in press..
- Kindle, J. C., H. E. Hurlburt, and E. J. Metzger, 1989: On the seasonal and interannual variability of the Pacific to Indian Ocean throughflow. *Proc. Western Pacific Int. Meeting and Workshop on TOGA COARE*, Noumea, New Caledonia, Centre ORSTOM de Noumea, 355–365..
- Kraus, E. B., and J. S. Turner, 1967: A one-dimensional model of the seasonal thermocline. II: The general theory and its consequences. *Tellus*, **19**, 98–106..
- LeBlond, P. H., and L. A. Mysak, 1978: *Waves in the Ocean*. Elsevier Oceanography Series, Vol. 20, Elsevier, 602 pp..
- Lukas, R., E. Firing, P. Hacker, P. L. Richardson, C. A. Collins, R. Fine, and R. Gammon, 1991: Observations of the Mindanao Current during the Western Equatorial Pacific Ocean Circulation Study. *J. Geophys. Res.*, **96**, 7089–7104..
- Madden, R. A., and P. R. Julian, 1994: Observations of the 40–50 day tropical oscillation—A review. *Mon. Wea. Rev.*, **122**, 814–837.. [Find this article online](#)
- Masumoto, Y., and T. Yamagata, 1993: Simulated seasonal circulation in the Indonesian seas. *J. Geophys. Res.*, **98**, 12 501–12 509..
- McCreary, J. P., and P. K. Kundu, 1989: A numerical investigation of sea surface temperature variability in the Arabian Sea. *J. Geophys. Res.*, **94**, 16 097–16 114..
- Meyers, G., 1996: Variation of Indonesian throughflow and the El Niño–Southern Oscillation. *J. Geophys. Res.*, **101**, 12 255–12 263..
- , R. J. Bailey, and A. P. Worby, 1995: Geostrophic transport of Indonesian throughflow. *Deep-Sea Res.*, **42**, 1163–1174..
- Miyama, T., T. Awaji, K. Akitomo, and N. Imasato, 1995: Study of seasonal transport variations in the Indonesian seas. *J. Geophys. Res.*, **100**, 20 517–20 541..
- Molcard, R., M. Fieux, J. C. Swallow, A. G. Ilahude, and J. Banjarnahor, 1994: Low frequency variability of the currents in Indonesian Channels (Savu-Roti and Roti-Ashmore Reef). *Deep-Sea Res.*, **41**, 1643–1662..
- , —, and A. G. Ilahude, 1996: The Indo–Pacific throughflow in the Timor Passage. *J. Geophys. Res.*, **101**, 12 411–12 420..
- Murray, S. P., and D. Arief, 1988: Throughflow into the Indian Ocean through the Lombok Strait, January 1985–January 1986. *Nature*, **333**, 444–447..
- Piola, A. R., and A. L. Gordon, 1984: Pacific and Indian Ocean upper-layer salinity budget. *J. Phys. Oceanogr.*, **14**, 747–753.. [Find this article online](#)
- Ponte, R. M., and D. S. Gutzler, 1992: 40–60 day oscillations in the western tropical Pacific: Results from an eddy-resolving global ocean model. *Geophys. Res. Lett.*, **19**, 1475–1478..
- Potemra, J. T., R. Lukas, and G. T. Mitchum, 1997: Large-scale estimation of transport from the Pacific to the Indian Ocean. *J. Geophys. Res.*, **102**, 27 795–27 812..
- Qiu, B., and R. Lukas, 1996: Seasonal and interannual variability of the North Equatorial Current, the Mindanao Current and the Kuroshio

Sadourny, R., 1975: The dynamics of finite-difference models of the shallow-water equations. *J. Atmos. Sci.*, **32**, 680–689.. [Find this article online](#)

Semtner, A. J., and R. M. Chervin, 1992: Ocean general circulation from a global eddy-resolving model. *J. Geophys. Res.*, **97**, 5493–5550..

Tsuchiya, M., R. Lukas, R. A. Fine, E. Firing, and E. Lindstrom, 1990: Source waters of the Pacific Equatorial Undercurrent. *Progress in Oceanography*, Vol. 23, Pergamon, 101–147..

Verschell, M. A., J. C. Kindle, and J. J. O'Brien, 1995: Effects of Indo–Pacific throughflow on the upper tropical Pacific and Indian Oceans. *J. Geophys. Res.*, **100**, 18 409–18 420..

Wajsowicz, R. C., 1994: A relationship between interannual variations in the South Pacific wind stress curl, the Indonesian Throughflow, and the west Pacific warm water pool. *J. Phys. Oceanogr.*, **24**, 2180–2187.. [Find this article online](#)

Watanabe, H., and Coauthors, 1997: Moored measurement of the Indonesian throughflow at the southwestern edge of the Philippine Sea. *Int. WOCE Newslett.*, **27**, 26–30..

Woodberry, K. E., M. E. Luther, and J. J. O'Brien, 1989: The wind-driven seasonal circulation in the southern tropical Indian Ocean. *J. Geophys. Res.*, **94**, 17 985–18 002..

Wyrki, K., 1987: Indonesian throughflow and the associated pressure gradient. *J. Geophys. Res.*, **92**, 12 941–12 946..

Yamagata, T., K. Mizuno, and Y. Masumoto, 1996: Seasonal variations in the equatorial Indian Ocean and their impact on the Lombok throughflow. *J. Geophys. Res.*, **101**, 12 465–12 473..

---

## Tables

Table 1. Parameter values for the base model run.

Parameter	Value
Initial upper-layer thickness	300 m
Minimum upper-layer thickness	80 m
Initial mixed layer depth	75 m
Minimum mixed layer depth	30 m
Gravity constant, $g$	$9.8 \text{ m s}^{-2}$
Thermal expansion coefficient $\alpha$	$0.00025^\circ\text{C}^{-1}$
Initial mixed layer temperature	$25^\circ\text{C}$
Initial fossil layer temperature	$15^\circ\text{C}$
Abyssal layer temperature $T_b$	$2^\circ\text{C}$
Relaxation timescale for $T_m, R_r$	40 days
Entrainment depth $H_e$	80 m
Entrainment timescale $t_e$	1 day
Horizontal eddy viscosity $A_h$	$400 \text{ m}^2 \text{ s}^{-1}$
Horizontal eddy diffusivity $K_h$	$400 \text{ m}^2 \text{ s}^{-1}$

[Click on thumbnail for full-sized image.](#)

---

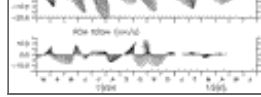
## Figures



[Click on thumbnail for full-sized image.](#)

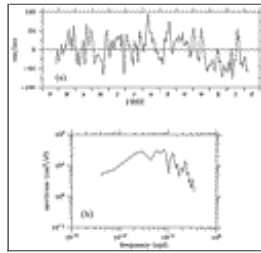
Fig. 1. Topography map in the region surrounding the Indonesian archipelago (based on NOAA's ETOP05 dataset). Solid contours denote the 3000-m isobaths.





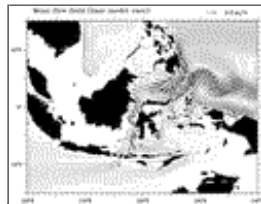
[Click on thumbnail for full-sized image.](#)

Fig. 2. Time series of velocity vectors from moored current meters deployed at the entrance of the Celebes Sea ( $4.0^{\circ}\text{N}$ ,  $127.5^{\circ}\text{E}$ ). (a) Observed velocity vectors at the 350-m and 550-m depths. (b) Velocity vectors after 30-to-120 day bandpass filtering. Adapted from [Watanabe et al. \(1997\)](#).



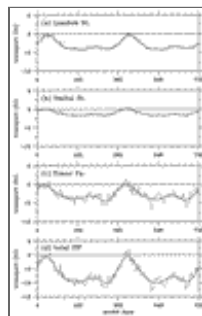
[Click on thumbnail for full-sized image.](#)

Fig. 3. (a) Time series of the first EOF mode for the alongchannel flow at  $11.3^{\circ}\text{S}$ ,  $122.9^{\circ}\text{E}$  in the Timor Passage (from [Fig. 9a](#) of [Molcard et al. 1996](#)). (b) Power spectra of the time series shown in variance preserving format.



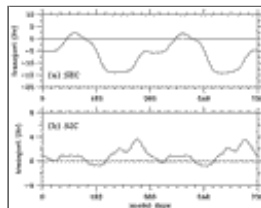
[Click on thumbnail for full-sized image.](#)

Fig. 4. Upper-layer mean flow pattern in the vicinity of the Indonesian archipelago. The flow pattern is derived from a global  $1\frac{1}{2}$ -layer reduced-gravity model ( $63^{\circ}\text{S}$ – $35^{\circ}\text{N}$ ) forced by the monthly climatological wind ([Hellerman and Rosenstein 1983](#)) and surface heat flux ([da Silva et al. 1994](#)). Areas shallower than 200 m are considered land in the model.



[Click on thumbnail for full-sized image.](#)

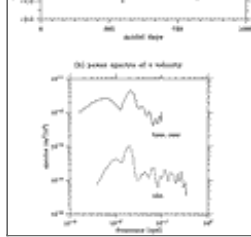
Fig. 5. Time series of model transport (dashed lines) through (a) the Lombok Strait, (b) the Ombai Strait, and (c) the Timor Passage over a 2-yr period. (d) The time series of the total throughflow transport. Base model result driven by climatological wind and heat flux data. Solid lines are the results after applying a 120-day low-pass filter.



[Click on thumbnail for full-sized image.](#)

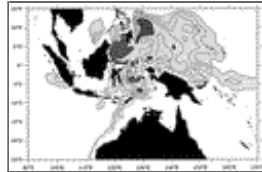
Fig. 6. Time series of transport of (a) the South Equatorial Current and (b) the South Java Current along  $104^{\circ}\text{E}$  in the eastern Indian Ocean. Here, SEC is defined as the zonal flow between  $15^{\circ}$  and  $9^{\circ}\text{S}$  and SJC is defined as the zonal flow between  $9^{\circ}\text{S}$  and the Java coast.





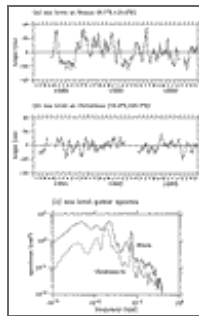
Click on thumbnail for full-sized image.

Fig. 7. (a) Time series of modeled meridional velocity at the entrance of the Celebes Sea ( $4.0^{\circ}\text{N}$ ,  $127.5^{\circ}\text{E}$ ) over a 3-yr period. (b) Power spectra of the meridional velocity time series from the base model (solid line) and from the current meter measurement at a 350-m depth (dashed line; cf. Fig. 2). Spectra are plotted in variance preserving format.



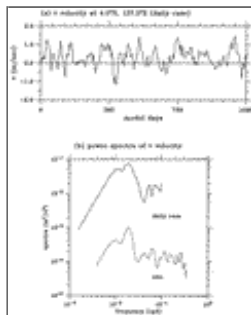
Click on thumbnail for full-sized image.

Fig. 8. Ratio of the eddy kinetic energy in the 30–60 day frequency band versus the total eddy kinetic energy from the base model run. Light-shaded areas denote the ratio greater than 5% and dark-shaded areas denote the ratio greater than 25%.



Click on thumbnail for full-sized image.

Fig. 9. Time series of the sea level anomalies observed at (a) Benoa and (b) Christmas tide gauge stations in the eastern Indian Ocean. (c) Power spectra of the Benoa and Christmas sea level time series in variance preserving format.



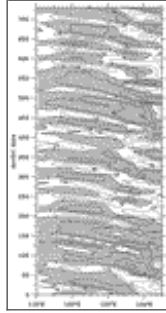
Click on thumbnail for full-sized image.

Fig. 10. (a) Time series of the meridional velocity at the entrance of the Celebes Sea ( $40^{\circ}\text{N}$ ,  $127.5^{\circ}\text{E}$ ). Daily model result. (b) Power spectra of the meridional velocity time series from the daily model (solid line) and from the current meter measurement at a 350-m depth (dashed line; cf. Fig. 2). Spectra are plotted in variance preserving format.



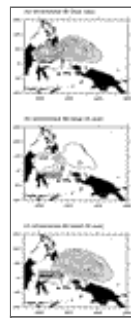
[Click on thumbnail for full-sized image.](#)

Fig. 11. Snapshots of the upper-layer thickness field from the base model output. Unit in meters. Each snapshot is separated by 10 days.



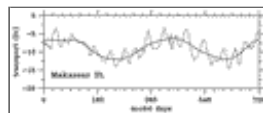
[Click on thumbnail for full-sized image.](#)

Fig. 12. Time–longitude diagram of the upper-layer thickness anomalies from the base model run along the center latitude (4°N) of the Celebes Sea. Unit in meters.



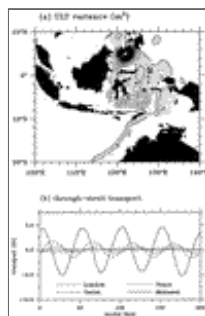
[Click on thumbnail for full-sized image.](#)

Fig. 13. Distributions of the eddy kinetic energy in the intraseasonal (30–60 day) frequency band from (a) the base model case, (b) the large Celebes Sea (CS) case, and (c) the small CS case. Unit in  $\text{m}^2 \text{s}^{-2}$ . The checkered blocks in (b) and (c) denote the Minahassa Peninsula shifted meridionally to test the Rossby wave resonance theory.



[Click on thumbnail for full-sized image.](#)

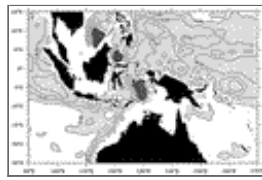
Fig. 14. Time series of transport (dashed line) through the Makassar Strait from the base model output. Solid line shows the result after applying a 120-day low-pass filter.



[Click on thumbnail for full-sized image.](#)

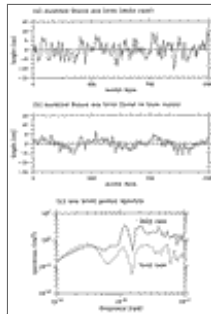
Fig. 15. (a) Distribution of the upper-layer thickness variance from a model driven by localized surface wind forcing. The model ocean has an initial constant depth of 300 m and is forced by an oscillatory zonal wind stress patch centered in the Celebes Sea:  $\tau^x = \tau_o \cos[\pi(x - x_c)/L_x] \exp[-y^2/2L_y^2] \sin(\omega t)$ ,  $-L_x/2 \leq x \leq L_x/2$ ;  $\tau^x = 0$  otherwise, where  $x_c = 122.5^\circ\text{E}$ ,  $L_x = 8^\circ$  long,  $y_c = 3.0^\circ\text{N}$ ,  $L_y = 4^\circ$  lat,  $\omega = 2\pi/50$  days, and  $\tau_o = 0.2 \text{ N m}^{-2}$ . Shaded areas denote variance values  $>2 \text{ m}^2$ . (b) Time series of flow transport through the four straits in this idealized model run.





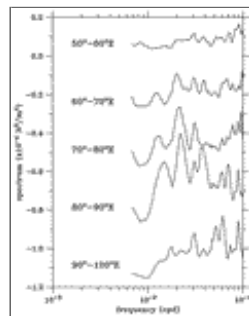
[Click on thumbnail for full-sized image.](#)

Fig. 16. Ratio of the eddy kinetic energy in the 30–60 day frequency band versus the total eddy kinetic energy from the daily model run. Light-shaded areas denote the ratio greater than 5% and dark-shaded areas denote the ratio greater than 25%.



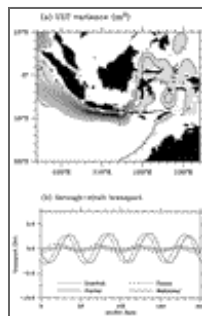
[Click on thumbnail for full-sized image.](#)

Fig. 17. Time series of modeled sea level anomalies at Benoa: (a) the daily model result and (b) the local (solid line) and base model (dashed line) results. Panel (c) shows the power spectra of the two time series in variance preserving format. Model day 0 here corresponds to 1 January 1985.



[Click on thumbnail for full-sized image.](#)

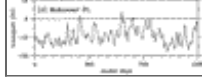
Fig. 18. Power spectra of the zonal wind stress in the intraseasonal frequency band (10–150 days) along the equator from 50° to 100°E. The power spectra are based on the daily 1000-mbar ECMWF wind data and are averaged in five 10°-wide segments. The power spectra for each segment are shown with an offset of  $0.3 \times 10^{-4} \text{ N}^2 \text{ m}^{-4}$ .



[Click on thumbnail for full-sized image.](#)

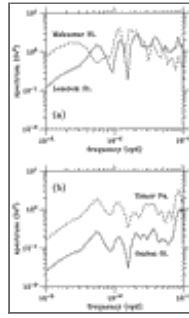
Fig. 19. Same as [Fig. 15](#) except for the oscillatory zonal wind stress patch in this case is centered in the equatorial eastern Indian Ocean, namely,  $x_c = 90.0^\circ\text{E}$ , and  $y_c = 0^\circ$ .





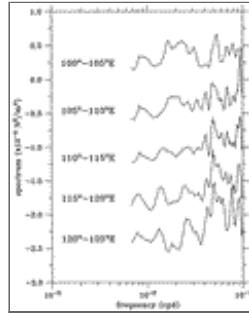
Click on thumbnail for full-sized image.

Fig. 20. Time series of the transport through (a) the Lombok Strait, (b) the Ombai Strait, (c) the Timor Passage, and (c) the Makassar Strait from the daily model run over a 3-yr period. Model day 0 here corresponds to 1 January 1985.



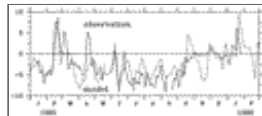
Click on thumbnail for full-sized image.

Fig. 21. Power spectra of the transport time series shown in [Fig. 20](#): (a) Lombok Strait vs Makassar Strait and (b) Timor Passage vs Ombai Strait.



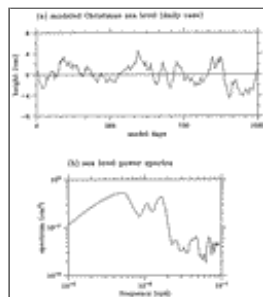
Click on thumbnail for full-sized image.

Fig. 22. Power spectra of the zonal wind stress in the intraseasonal frequency band (10–150 days) along the Indonesian coast from 100° to 125°E. The power spectra are based on the daily 1000-mbar ECMWF wind data and are averaged in five 5°-wide segments. The power spectra for each segment are shown with an offset of  $0.7 \times 10^{-4} \text{ N}^2 \text{ m}^{-4}$ .



Click on thumbnail for full-sized image.

Fig. 23. Time series of the observed meridional flow (solid line) versus the modeled meridional transport (dashed line) through the Lombok Strait. The observed time series is based on [Fig. 3](#) of [Murray and Arief \(1988\)](#) and the modeled time series is from the daily model case. The unit for y axis is Sv for the model transport and  $0.1 \text{ m s}^{-1}$  for the observed meridional flow.



Click on thumbnail for full-sized image.

Fig. 24. (a) Time series of modeled sea level anomalies at Christmas Island. (b) Power spectra of the time series in variance preserving format. Model day 0 here corresponds to 1 January 1985.

<sup>1</sup> The width of the Lombok Strait is 40 km, which is about one-third of the size of the local, first-mode baroclinic Rossby radius.

<sup>2</sup> The intraseasonal signals in the Ombai Strait bear similar characteristics to those in the Timor Passage, but with a much lower energy level. Our discussion below will focus on the Timor Passage only.

\* Current affiliation: Japan Marine Science and Technology Center, Yokosuka, Japan.

*Corresponding author address:* Dr. Bo Qiu, Department of Oceanography, University of Hawaii at Manoa, 1000 Pope Road, Honolulu, HI 96822.

E-mail: [bo@lunarmax.soest.hawaii.edu](mailto:bo@lunarmax.soest.hawaii.edu)

top ▲



© 2008 American Meteorological Society [Privacy Policy and Disclaimer](#)  
Headquarters: 45 Beacon Street Boston, MA 02108-3693  
DC Office: 1120 G Street, NW, Suite 800 Washington DC, 20005-3826  
[amsinfo@ametsoc.org](mailto:amsinfo@ametsoc.org) Phone: 617-227-2425 Fax: 617-742-8718  
[Allen Press, Inc.](#) assists in the online publication of *AMS* journals.